Nonvolatile Electrical Control of Transport Properties in Multiferroic $OsCl_2/Sc_2CO_2$ Heterostructure

Shi-Xu Wang(王士序)[1], Shu-Xiang Qiao(乔树祥)[1], Mei-Yan Ni(倪美燕)[1*], Xiao-Hong Zheng(郑小宏)[2], Hua Hao(郝华)[3], Hong-Yan Lu(路洪艳)[1*], and Ping Zhang(张平)[1,4*]

[1]*School of Physics and Physical Engineering, Qufu Normal University, Qufu 273165, China*
[2]*College of Information Science and Technology, Nanjing Forestry University, Nanjing 210037, China*
[3]*School of Physics, Hangzhou Normal University, Hangzhou 311121, China*
[4]*Institute of Applied Physics and Computational Mathematics, Beijing 100088, China*

(Received 3 April 2025; accepted manuscript online 30 May 2025)

Ferromagnetic materials play an important role in memory materials, but conventional control methods are often limited by issues such as high power consumption and volatility. Multiferroic heterostructures provide a promising alternative to achieve low power consumption and nonvolatile electric control of magnetic properties. In this paper, a two-dimensional multiferroic van der Waals heterostructure $OsCl_2/Sc_2CO_2$, which is composed of ferromagnetic monolayer $OsCl_2$ and ferroelectric monolayer Sc_2CO_2, is studied by first-principles density functional theory. The results show that by reversing the direction of the electric polarization of Sc_2CO_2, $OsCl_2$ can be transformed from a semiconductor to a half-metal, demonstrating a nonvolatile electrical manipulation of the heterostructure through ferroelectric polarization. The underlying physical mechanism is explained by band alignments and charge density differences. Furthermore, based on the heterostructure, we construct a multiferroic tunnel junction with a tunnel electroresistance ratio of $3.38 \times 10^{14}\%$ and a tunnel magnetoresistance ratio of $5.04 \times 10^{6}\%$, allowing control of conduction states via instantaneous electric or magnetic fields. The findings provide a feasible strategy for designing advanced nanodevices based on the giant tunnel electroresistance and tunnel magnetoresistance effects.

DOI: 10.1088/0256-307X/42/8/080701 CSTR: 32039.14.0256-307X.42.8.080701

1. Introduction. With the discovery of graphene,[1] materials science enters a new era characterized by the exploration of two-dimensional (2D) materials. This has led researchers to predict and discover a wide range of novel 2D materials. These 2D materials exhibit unique quantum behavior at the atomic scale and exhibit properties not observed in their bulk counterparts.[2–6] Among these 2D materials, 2D ferromagnetic (FM) materials are particularly important in the research of transport devices because of their reduced thickness and enhanced suitability for device manufacturing. However, for a long time, magnetic materials have been relatively scarce among the predicted 2D materials, and their experimental synthesis has also been limited.[7–13] Major breakthroughs were achieved by Zhang's group and Xu's group, who experimentally observed intrinsically FM behavior in bilayer $Cr_2Ge_2Te_6$[14] and monolayer CrI_3,[15] respectively. Subsequently, 2D van der Waals (vdW) magnetic materials have attracted significant attention.[4,5,16,17] Many excellent properties have been explored, such as magnetic anisotropy energy (MAE),[18–20] valley polarization,[21,22] altermagnetism,[23–25] transport properties,[26–28], etc. To explore novel properties of magnetic materials and extend their application, many methods have been proven to be effective, such as magnetic field, electric field, strain, doping, and light.[29–34] Nevertheless, these control methods are volatile, relying on continuous external stimuli such as electric, magnetic, or mechanical stress. Once the external conditions are removed, the induced state of the FM material reverts to its original state. This not only leads to significant, constant energy consumption but also compromises control stability. Therefore, there is a critical need to develop nonvolatile control methods to address these limitations.

Magnetoelectric coupling in multiferroic heterostructures (HSs) that combine FM and ferroelectric (FE) materials offers a novel approach to achieve low power consumption and nonvolatile electric control of magnetic properties.[35–38] Theoretically, some HSs have been proposed for nonvolatile switching of FM states, such as CrI_3/Sc_2CO_2,[39] $Cr_2Ge_2Te_6/Sc_2CO_2$,[40] $MnCl_3/CuInP_2S_6$,[41] $LaBr_2/\alpha$-In_2Se_3,[26] and $RuCl_2/Al_2S_3$,[42] which demonstrate the feasibility of this approach. FE materials exhibit spontaneous electric polarization within specific temperature ranges, with two stable polarization states ($P\uparrow$ and $P\downarrow$).[43–50] The spontaneous electric polarization generates an electric field that can be used to control the mag-

*Corresponding authors. Email: nimy@qfnu.edu.cn; hylu@qfnu.edu.cn; zhang_ping@iapcm.ac.cn
© 2025 Chinese Physical Society and IOP Publishing Ltd. All rights, including for text and data mining, AI training, and similar technologies, are reserved.

netic material in the HS.[51,52] Through the application of brief electric pulses to switch the polarization direction of the FE material, the resulting electric field acting on the adjacent FM material can be precisely controlled. This mechanism enables nonvolatile electric control of the FM material's magnetic properties, including magnetization orientation, without the need for continuous external energy input. Thus, we attempt to construct HSs to achieve nonvolatile electric control of FM materials.

In this work, we construct a 2D multiferroic vdW HS $OsCl_2/Sc_2CO_2$ consisting of the FE monolayer Sc_2CO_2[43,46] and the FM monolayer $OsCl_2$.[21] $OsCl_2$ exhibits a remarkably high Curie temperature (T_C = 495 K)[21] that significantly surpasses those of monolayer CrI_3 (T_C = 45 K)[15] and bilayer $Cr_2Ge_2Te_6$ (T_C = 28 K),[14] enabling room-temperature device operation without cryogenic constraints. This overcomes fundamental limitations in existing 2D spintronic materials. Besides, unlike the in-plane ferromagnetism of $Cr_2Ge_2Te_6$, $OsCl_2$ maintains robust out-of-plane FM ordering, which is essential for vertical spin transport in practical magnetic tunnel junctions (MFTJs). Our results demonstrate that $OsCl_2$ can be transformed from a semiconductor to a half-metal by reversing the FE polarization direction in Sc_2CO_2. This intriguing phenomenon can be understood through changes in band alignment and charge redistribution under different FE polarization states. In addition, the transport properties of a MFTJ exhibit giant tunnel electroresistance (TER) and tunnel magnetoresistance (TMR) ratios of 3.38×10^{14}% and 5.04×10^{6}%, respectively, in the MFTJ, which is of great significance for application of HSs in spintronic devices.

2. Computational Methods. In this work, structural relaxation and electronic property calculations are performed using density functional theory (DFT),[53] implemented in the Vienna *ab initio* simulation package (VASP) code.[54] The projector-augmented wave method is employed to describe the electron–ion interaction.[55,56] The Perdew–Burke–Ernzerhof (PBE) generalized gradient approximation is adopted to describe the exchange-correlation functional.[57] We employ the Hubbard model to account for the strong on-site interactions of localized d electrons in osmium (Os) and scandium (Sc) atoms, with U = 2.0 eV and J = 0.0 eV for the d orbitals of both elements.[21,40] Heyd–Scuseria–Ernzerhof (HSE06) hybrid functional is used to obtain the accurate band structures.[58] The cut-off energy is set to 500 eV, and the convergence criteria for the energy and force are 10^{-6} eV and 0.01 eV·Å^{-1}, respectively. We use the DFT-D3 method to account for vdW interactions.[59] The interlayer vacuum of 15 Å is applied in the out-of-plane direction to avoid the artificial interaction between periodic images. A Monkhorst-Pack k-mesh grid of $12\times12\times1$ is used for Brillouin zone sampling.[60] Transport calculations are performed using the Atomistix ToolKit (ATK) package,[61] which combines DFT with the non-equilibrium Green's function technique.[62] For transport calculations, a k-point grid of $21\times1\times201$ is used for self-consistency in the first Brillouin zone of the electrodes, while a denser grid of $121\times1\times1$ is employed for transmission calculations.

3. Structural and Electronic Properties of Isolated $OsCl_2$ and Sc_2CO_2 Monolayers. The crystal structure of monolayer $OsCl_2$ is shown in Fig. 1(a), which consists of Cl-Os-Cl sandwich layers with the space group D_{3h} in the 2H phase. At the PBE+U level, the calculated lattice constant of $OsCl_2$ monolayer is $a = b = 3.47$ Å and the length of Os-Cl bond is 2.61 Å. In order to determine the magnetic ground state, a $1\times2\sqrt{3}\times1$ supercell is constructed. Three different configurations including FM, zigzag-type antiferromagnetic (AFMz), and stripe-type antiferromagnetic (AFMs) configurations are investigated, as shown in Fig. S1 of the Supplementary Materials (SM). The total energy differences between the antiferromagnetic (AFM) states and the FM state ($\Delta E = E_{AFM} - E_{FM}$) are listed in Table 1. Positive values indicate that the magnetic ground state of the $OsCl_2$ monolayer is the FM configuration. The net magnetic moment is 4 μ_B/Os atom corresponding to a high spin state of the d^6 electron configuration, which is consistent with previous reports.[21,22] Further, the band structure of the $OsCl_2$ is calculated, which shows that $OsCl_2$ is a semiconductor with a band gap of 0.84 eV. The conduction band minimum (CBM) and the valence band maximum (VBM) are both occupied by the spin-down channel, as depicted in Fig. 1(b). The band properties of $OsCl_2$ are consistent with those reported in previous studies.[21] As shown in Fig. S2(a) of the SM, the band structure predicted by the HSE06 functional agrees well with that from the PBE+U functional, validating the reliability of our calculations. In addition, we also calculate the phonon dispersion of $OsCl_2$ monolayer as shown in Fig. 1(c). The absence of imaginary frequencies in the entire Brillouin zone confirms the dynamic stability of $OsCl_2$ monolayer.

For the Sc_2CO_2 monolayer, its crystal structure is shown in Fig. 1(d), featuring a hexagonal lattice with the space group $P3m1$. A quintuple layer is built up in the sequence of O-Sc-C-Sc-O, characteristic of the layered structure of MXene.[38,46] The lattice constant of Sc_2CO_2 monolayer is $a = b = 3.41$ Å.[39] Due to the asymmetric displacement of the central C atomic layer, Sc_2CO_2 exhibits stable out-of-plane electrical polarization, behaving as a 2D FE material. When the middle C atom aligns vertically with the top O layer, the polarization state is denoted as $P\uparrow$; when it aligns with the lower O layer, the polarization state is denoted as $P\downarrow$,[46] as shown in Fig. 1(d). The band structure of Sc_2CO_2 [Fig. 1(e)] reveals that the Sc_2CO_2 monolayer is a semiconductor with a band gap of 1.91 eV, consistent with the reported value of 1.78 eV.[40] The accurate band structure of Sc_2CO_2 is also calculated using the HSE06 method, as shown in Fig. S2(b) of the SM, which closely matches that from the PBE+U functional. Furthermore, the phonon spectrum of Sc_2CO_2 [Fig. 1(f)] demonstrates its dynamic stability, with negligible imaginary frequencies throughout the Brillouin zone.

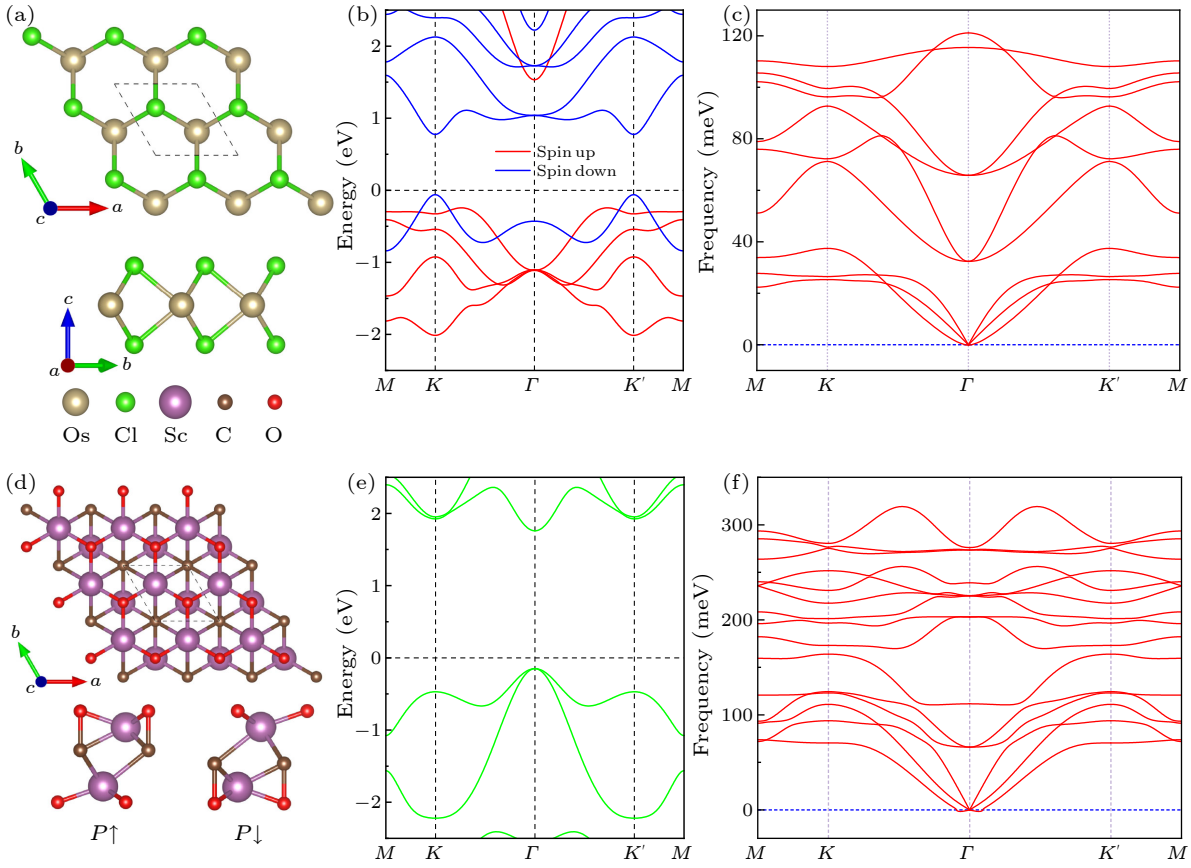

Fig. 1. (a) Top and side views of the crystal structure for the FM $OsCl_2$ monolayer. (b) Spin-resolved band structures of the $OsCl_2$ monolayer. The Fermi level is set to zero. (c) Phonon spectrum of the monolayer $OsCl_2$. (d)–(f) Similar to (a)–(c), but for FE Sc_2CO_2 monolayer.

4. Structural and Electronic Properties of $OsCl_2/Sc_2CO_2$ HS. Considering that the lattice constant of monolayer $OsCl_2$ is similar to that of monolayer Sc_2CO_2, with a lattice mismatch of 1.73%, the $OsCl_2/Sc_2CO_2$ HS is constructed in a unit-cell configuration. To minimize additional strain effects and maintain the intrinsic properties of $OsCl_2$ as much as possible, the same lattice parameter as the $OsCl_2$ monolayer is adopted for the $OsCl_2/Sc_2CO_2$ HS. All HSs were relaxed with fixed lattice parameters while fully optimizing atomic positions. As shown in Fig. S3 of the SM, six typical stacking configurations are considered for each electrical polarization. The total energies and interlayer distances for different configurations are listed in Table S1 of the SM. For both electrical polarization states, the most stable stacking structures are Type-I, with the lowest total energies. The top and side views of the crystal structures are shown in Figs. 2(a) and 2(b) with the electrical polarization $P\uparrow$ and $P\downarrow$, respectively. In the Type-I configuration, the Cl atoms of $OsCl_2$ locate below the lower Sc atoms of Sc_2CO_2 for both $P\uparrow$ and $P\downarrow$ polarization states. We calculated the total energies for the Type-I configuration with different magnetic orderings (FM, AFMz, and AFMs), as listed in Table 1, confirming the FM state as the magnetic ground state of the HS.

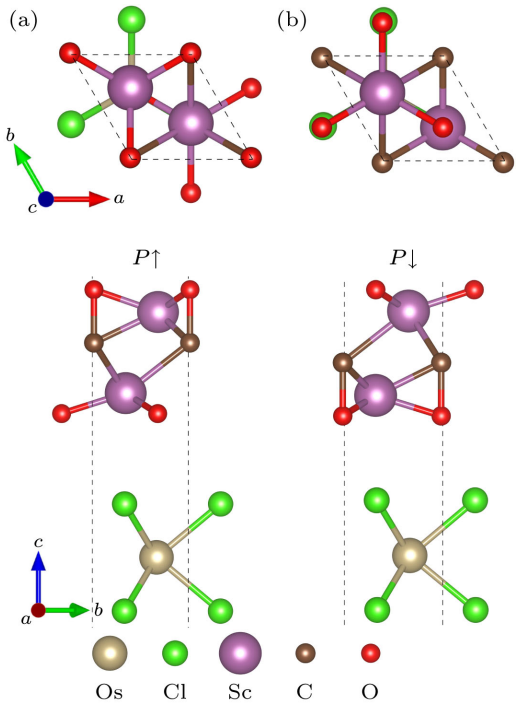

Fig. 2. Top and side views of the $OsCl_2/Sc_2CO_2$ HS in Type-I configuration with upward and downward polarization states of Sc_2CO_2 ($P\uparrow$ and $P\downarrow$).

Table 1. The energy differences (eV) of FM, AFMz, and AFMs relative to FM and MAE (meV) for $OsCl_2$ and the HS.

System	ΔE_{FM}	ΔE_{AFMz}	ΔE_{AFMs}	MAE
$OsCl_2$	0	0.557	1.053	28.897
Type-I $P\uparrow$	0	0.555	1.049	30.021
Type-I $P\downarrow$	0	0.502	1.000	40.976

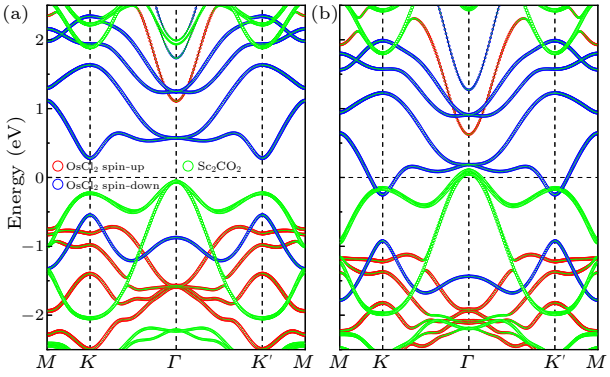

Fig. 3. Projected band structures of the $OsCl_2/Sc_2CO_2$ vdW HS with the Type-I stacking configuration for (a) the $P\uparrow$ polarized state and (b) the $P\downarrow$ polarized state. Here, red and blue symbols denote the contributions from spin-up and spin-down states of $OsCl_2$, respectively, and green represents the contributions of Sc_2CO_2.

Next, we investigate the electronic properties of the $OsCl_2/Sc_2CO_2$ HS. The projected band structures of $OsCl_2/Sc_2CO_2$ with Type-I stacking are shown in Fig. 3. The band structure of the $OsCl_2/Sc_2CO_2$ HS in the $P\uparrow$ state is shown in Fig. 3(a), indicating that the HS is a semiconductor with an indirect band gap of 0.33 eV. The CBM is contributed by the spin-down channel of $OsCl_2$, while the VBM is contributed by Sc_2CO_2. When the HS is switched to the $P\downarrow$ state, the corresponding band structure is shown in Fig. 3(b). Compared with the $P\uparrow$ state, in the $P\downarrow$ state, the band of $OsCl_2$ shifts downward, and the band of Sc_2CO_2 shifts upward, with the Fermi level crossing both the CBM and VBM. Specifically, the CBM is contributed by the spin-down channel of $OsCl_2$, while the VBM is contributed by Sc_2CO_2. Therefore, the HS changes to a metallic state, with $OsCl_2$ exhibiting half-metallic behavior. The electronic structures obtained from the HSE06 functional (Fig. S4 of the SM) are in excellent agreement with those from the PBE+U functional, further confirming the accuracy of the band structures. We also calculated the band structures for five other configurations, shown in the Figs. S5–S9 of the SM. The semiconductor-to-metal transition in these configurations is similar to that in Type-I. In the $P\uparrow$ state, all configurations exhibit semiconducting behavior with varying band gaps, as shown in Table S1 of the SM. In the $P\downarrow$ state, the HS transforms into a metallic state, with $OsCl_2$ displaying half-metallic behavior. Notably, both $P\uparrow$ and $P\downarrow$ states of Sc_2CO_2 remain stable without external fields, enabling nonvolatile switching between semiconducting and half-metallic states in $OsCl_2$.

The HS demonstrates switchable semiconducting-to-metallic transition under different electrical polarization conditions. To understand the physical mechanism of this switching behavior, band alignment and charge density difference are investigated. As shown in Fig. 4(a), $OsCl_2$ has a symmetric average electrostatic potential in the out-of-plane direction. In contrast, due to the breaking of spatial symmetry, Sc_2CO_2 exhibits a potential energy difference of 3.12 eV between its two sides. When $OsCl_2$ monolayers contact Sc_2CO_2 in different polarization states, different band alignments between $OsCl_2$ and Sc_2CO_2 are shown in Fig. 4(b). For the HS in the $P\uparrow$ state, the VBM of Sc_2CO_2 lies below the CBM of $OsCl_2$, inhibiting charge transfer

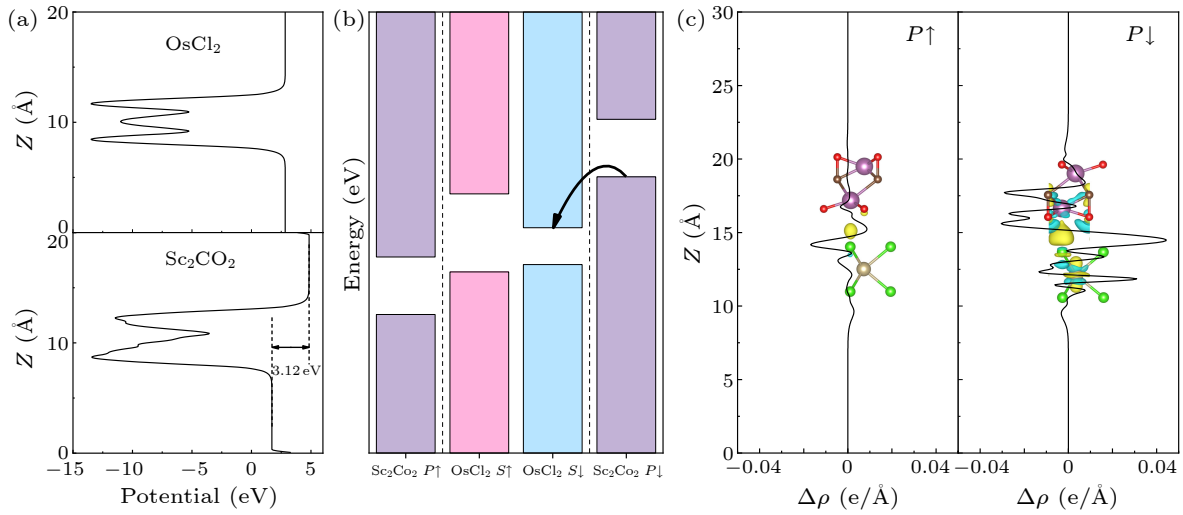

Fig. 4. (a) Plane average electrostatic potential along the z direction of the $OsCl_2$ monolayer (upper panel) and Sc_2CO_2 monolayer (lower panel). (b) Band alignments for the Type-I stacking the $OsCl_2/Sc_2CO_2$ HS with different polarization orientations. All the energy levels are shifted relative to the vacuum level of $OsCl_2$. (c) The plane average charge density difference along z of Type-I stacking of the $OsCl_2/Sc_2CO_2$ HS with $P\uparrow$ and $P\downarrow$ polarized states.

between the two adjacent layers. Therefore, the HS retains its semiconducting property. For the HS in the $P\downarrow$ state, the VBM of Sc_2CO_2 is located above the CBM of $OsCl_2$, facilitating electron transfer from Sc_2CO_2 into $OsCl_2$. The charge transfer can also be represented by the charge density difference, as illustrated in Fig. 4(c). In the $P\uparrow$ state, the charge transfer between $OsCl_2$ and Sc_2CO_2 is negligible. At the heterointerface in the $P\downarrow$ state, significant charge transfer occurs from the conduction band of $OsCl_2$ to the valence band of Sc_2CO_2. Thus, a more pronounced modification in the band structure is observed in the $P\downarrow$ state. This result is consistent with the band structures in Fig. 3(b), where the Fermi level crosses the VBM of Sc_2CO_2 and the CBM of $OsCl_2$, resulting in the metallicity of the HS.

5. MAE of $OsCl_2/Sc_2CO_2$ HS. The MAE is the energy difference of a ferromagnet when the saturation magnetization vector is oriented along different directions. Considering spin–orbit coupling, the MAE is defined as

$$\mathrm{MAE} = E_x - E_z, \tag{1}$$

where E_x and E_z correspond to the total energy of the structure with the magnetic axis oriented in-plane and out-of-plane, respectively. A negative (positive) MAE value means that the easy magnetization axis is oriented in the in-plane (out-of-plane) direction. As shown in Table 1, the easy magnetization axis of both the $OsCl_2$ monolayer and the $OsCl_2/Sc_2CO_2$ HS is oriented along the z-axis, indicating the out-of-plane magnetization. Numerically, the MAE of the $OsCl_2/Sc_2CO_2$ HS in the $P\uparrow$ state is comparable to that of the isolated $OsCl_2$ monolayer. Upon polarization reversal, the MAE exhibits a slight increase. We also investigated MAE for five other configurations of the $OsCl_2/Sc_2CO_2$ HS, as summarized in Table S1 of the SM. The HS exhibits slightly larger MAE values compared to the $OsCl_2$ monolayer. Additionally, for the HS, the MAE in the $P\uparrow$ state is smaller than that in the $P\downarrow$ state.

To understand the MAE variation under different polarization states, we focused on the Type-I HS configuration. Figure S10 of the SM compares the orbital-resolved MAE of $OsCl_2/Sc_2CO_2$ under two polarization states with that of an isolated $OsCl_2$ monolayer. The results demonstrate that both d and p orbitals of Os atoms make positive contributions to the MAE, with the d orbital being the dominant contributor. This explains the out-of-plane magnetization preference in these systems. In the $OsCl_2/Sc_2CO_2$ $P\downarrow$ configuration, both positive and negative MAE contributions decrease compared to other configurations, except for the negative contribution from the d_{xz} and d_{yz} orbitals, which increases. Notably, the reduction in the negative contribution is more pronounced than that of the positive contribution, leading to a net MAE enhancement. Figures S10(d)–S10(f) of the SM indicate that the MAE differences between polarization states primarily stem from interactions between the d_{xy} and $d_{x^2-y^2}$, d_{xz} and d_{z^2} orbitals. While these interactions remain stable in the $P\uparrow$ configuration (similar to the isolated $OsCl_2$ monolayer), the $P\downarrow$ configuration exhibits significant suppression of the d_{xy} and $d_{x^2-y^2}$ coupling and a sign reversal (to positive) for the d_{xz} and d_{z^2} interaction.

6. Transport Properties of $OsCl_2/Sc_2CO_2$ MFTJ. Given the remarkable electronic properties of the $OsCl_2/Sc_2CO_2$ HS, we constructed the MFTJ as shown in Fig. 5. The left and right leads (indicated by dashed boxes) are composed of the smallest rectangular supercells of the $OsCl_2/Sc_2CO_2$ HS. The central region comprises two supercells of $OsCl_2$ as the channel region, flanked by three supercells of $OsCl_2/Sc_2CO_2$ vdW HS on the left and right sides as buffer regions, respectively. The transport properties of this MFTJ can be modulated via two distinct mechanisms. The first approach maintains the initial parallel (P) magnetization state while reversing the FE polarization directions between $P\downarrow$ state and $P\uparrow$ state in the MFTJ through an applied electric field pulse. The second method maintains the initial polarization direction ($P\downarrow$ state) and applies selective magnetic fields to control the magnetization alignment of the electrodes, allowing transitions between P and anti-parallel (AP) configurations. The TER and TMR are then investigated in the MFTJ. The tunneling equilibrium conductance of the system can be obtained by

$$G = G_0 \sum_{k_x} T(k_x, E), \tag{2}$$

where $T(k_x, E)$ is the transmission function of the electronic state at $k = k_x$ for energy E, and $G_0 = 2e^2/h$ is the conductance quantum. Based on this, the TER ratio of the system is defined as [63]

$$\mathrm{TER} = \frac{|G\uparrow - G\downarrow|}{\min(G\uparrow, G\downarrow)} \times 100\%, \tag{3}$$

where $G\uparrow$ and $G\downarrow$ represent the tunneling equilibrium conductance of the MFTJ when the FE layer is in the $P\uparrow$ and $P\downarrow$ states, respectively. The TMR ratio is calculated by [64]

$$\mathrm{TMR} = \frac{G_\mathrm{P} - G_\mathrm{AP}}{G_\mathrm{AP}} \times 100\%, \tag{4}$$

where G_P and G_AP denote the tunneling equilibrium conductance of the MFTJ with the two leads in the P magnetization and AP magnetization states, respectively.

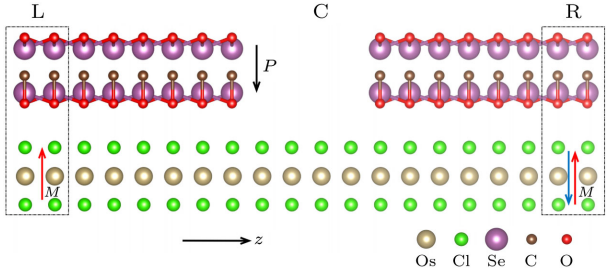

Fig. 5. The structure of the MFTJ constructed with the $OsCl_2/Sc_2CO_2$ vdW HS.

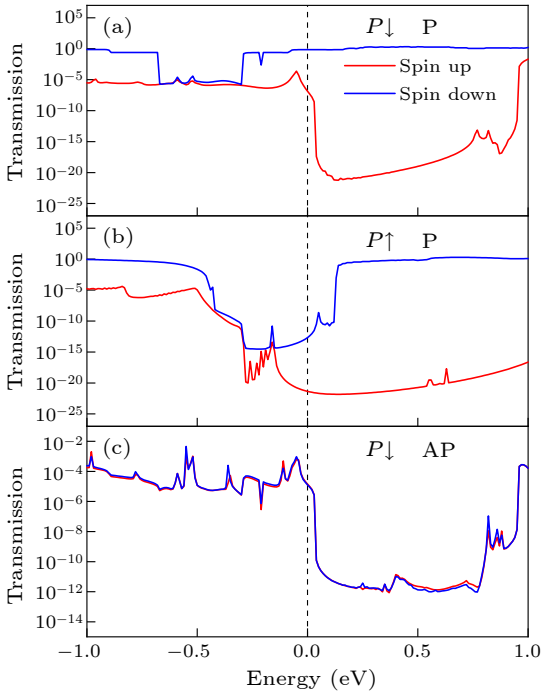

Fig. 6. The transmission function of the MFTJ in (a) $P\downarrow$ polarization and P magnetization configuration; (b) $P\uparrow$ polarization and P magnetization configuration; (c) $P\downarrow$ polarization and AP magnetization configuration. The spin-up and spin-down transmissions are represented by red and blue lines, respectively.

The spin-dependent transmission spectra of the MFTJ under different FE polarization and magnetization configurations are shown in Fig. 6. Figure 6(a) displays the transmission function for the MFTJ in the $P\downarrow$ polarization state with P magnetization configuration. At the Fermi level, the transmission coefficient in the spin-up channel is negligible with $T_{\rm UP} = 1.362 \times 10^{-7}$, while that in the spin-down channel is significantly larger with $T_{\rm DN} = 0.717$. This results in nearly 100% spin polarization, thereby realizing half-metallic transport properties. When the polarization direction is reversed with P magnetization maintained, both spin channels exhibit strongly suppressed conduction at the Fermi level with $T_{\rm UP} = 4.420 \times 10^{-22}$ and $T_{\rm DN} = 2.121 \times 10^{-13}$ respectively, as shown in Fig. 6(b). This behavior is in complete agreement with the band structure depicted in Fig. 3(a). Comparing $P\downarrow$ and $P\uparrow$ polarizations under the P magnetization configuration, the MFTJ achieves a remarkable TER ratio of up to 3.38×10^{14}%.

In the $P\downarrow$ polarization configuration, magnetization reversal of the right lead via magnetic field application to achieve AP alignment nearly completely suppresses transmission throughout the investigated energy range. At the Fermi level, the transmission coefficients in spin-up and spin-down channels are $T_{\rm UP} = 1.424 \times 10^{-5}$ and $T_{\rm DN} = 1.287 \times 10^{-5}$, respectively. Compared with the P magnetization configuration in the $P\downarrow$ polarization state, the MFTJ demonstrates an extraordinary TMR ratio of 5.04×10^{6}%. These results demonstrate that the conduction states of the MFTJ can be manipulated by instantaneous electric or magnetic fields, offering enhanced versatility for designing high-performance multifunctional MFTJs.

7. Conclusion. In summary, based on first-principles calculation, we have successfully constructed a 2D multiferroic vdW $OsCl_2/Sc_2CO_2$ HS, composed of the FM $OsCl_2$ monolayer and the FE Sc_2CO_2 monolayer, and achieved nonvolatile electrical control of the HS through FE polarization. Specifically, when Sc_2CO_2 is in the $P\uparrow$ state, the HS is a semiconductor, while in the $P\downarrow$ state, the HS becomes metallic, and the $OsCl_2$ sublayer exhibits half-metallic behavior. The underlying mechanism is explained through band alignment and charge density difference analysis. The MAE variations of both the HS under two FE polarization states and the $OsCl_2$ monolayer were further investigated. Furthermore, we investigated the transport properties of the MFTJ based on the $OsCl_2/Sc_2CO_2$ HS and found that giant TER and TMR were achieved, with TER and TMR ratios reaching 3.38×10^{14}% and 5.04×10^{6}%, respectively. Our results demonstrate that the vdW HS combining ferromagnetism and ferroelectricity exhibits new physical properties through magnetoelectric coupling, which offers a novel approach for developing 2D storage and transport devices, as well as creating more possibilities for the development of high-performance spintronic nanodevices.

Acknowledgements. This work was supported by the National Natural Science Foundation of China (Grant Nos. 12074213, 11574108, and 12104253), the National Key R&D Program of China (Grant No. 2022YFA1403103), the Major Basic Program of the Natural Science Foundation of Shandong Province (Grant No. ZR2021ZD01), the Natural Science Foundation of Shandong Provincial (Grant No. ZR2023MA082), and the Project of Introduction and Cultivation for Young Innovative Talents in Colleges and Universities of Shandong Province.

References

[1] Novoselov K S, Geim A K, Morozov S V, Jiang D D, Katsnelson M I, Grigorieva I V, Dubonos S V, and Firsov A A 2005 *Nature* **438** 197
[2] An Y P, Hou Y S, Wang H, Li J, Wu R Q, Wang T X, Da H X, and Jiao J T 2019 *Phys. Rev. Appl.* **11** 064031
[3] Huang C X, Feng J S, Wu F, Ahmed D, Huang B, Xiang H J, Deng K M, and Kan E J 2018 *J. Am. Chem. Soc.* **140** 11519
[4] Zeng M Q, Xiao Y, Liu J X, Yang K N, and Fu L 2018 *Chem. Rev.* **118** 6236
[5] Bonilla M, Kolekar S, Ma Y J, Diaz H C, Kalappattil V, Das R, Eggers T, Gutierrez H R, Phan M H, and Batzill M 2018 *Nat. Nanotechnol.* **13** 289
[6] Ribeiro-Palau R, Zhang C J, Watanabe K, Taniguchi T, Hone J, and Dean C R 2018 *Science* **361** 690
[7] Kimura T, Goto T, Shintani H, Ishizaka K, Arima T H, and Tokura Y 2003 *Nature* **426** 55
[8] Shannon N, Momoi T, and Sindzingre P 2006 *Phys. Rev. Lett.* **96** 027213
[9] Ando K 2006 *Science* **312** 1883
[10] Neumaier D, Schlapps M, Wurstbauer U, Sadowski J, Reinwald M, Wegscheider W, and Weiss D 2008 *Phys. Rev. B* **77** 041306

[11] Zhou P, Sun C Q, and Sun L Z 2016 *Nano Lett.* **16** 6325
[12] Wu Q S, Zhang J J, Hao P P, Ji Z Y, Dong S, Ling C Y, Chen Q, and Wang J L 2016 *J. Phys. Chem. Lett.* **7** 3723
[13] Bruno P 2001 *Phys. Rev. Lett.* **87** 137203
[14] Gong C, Li L, Li Z L, Ji H W, Stern A, Xia Y, Cao T, Bao W, Wang C Z, Wang Y, Qiu Z Q, Cava R J, Louie S G, Xia J, and Zhang X 2017 *Nature* **546** 265
[15] Huang B, Clark G, Moratalla E N, Klein D R, Cheng R, Seyler K L, Zhong D, Schmidgall E, McGuire M A, Cobden D H *et al.* 2017 *Nature* **546** 270
[16] Liu Y, Guo J, Zhu E, Liao L, Lee S J, Ding M N, Shakir I, Gambin V, Huang Y, and Duan X F 2018 *Nature* **557** 696
[17] Unuchek D, Ciarrocchi A, Avsar A, Watanabe K, Taniguchi T, and Kis A 2018 *Nature* **560** 340
[18] Zuo P J, Wang H, Wang Z, and Wu R Q 2020 *J. Magn. Magn. Mater.* **506** 166796
[19] Xie W F, Xu X, Li M, and Wang H 2023 *J. Magn. Magn. Mater.* **573** 170662
[20] Abdullah, Rahman A U, Tumelero M A, Liao J J, Magalhaes S G, Amin M A, and Guo G H 2025 *Phys. Chem. Chem. Phys.* **27** 8833
[21] Xie W F, Zhang L, Yue Y L, Li M, and Wang H 2024 *Phys. Rev. B* **109** 024406
[22] Zhou Y, Ye H S, Zhang J T, and Dong S 2024 *Phys. Rev. Mater.* **8** 104403
[23] Zeng S K and Zhao Y J 2024 *Phys. Rev. B* **110** 054406
[24] Pan B R, Zhou P, Lyu P B, Xiao H P, Yang X J, and Sun L Z 2024 *Phys. Rev. Lett.* **133** 166701
[25] Jiang B, Hu M Z, Bai J L, Song Z Y, Mu C, Qu G X, Li W, Zhu W L, Pi H Q, Wei Z X, Sun Y J, Huang Y B, Zheng X Q, Peng Y Y, He L H, Li S L, Luo J L, Li Z, Chen G F, Li H, Weng H M, and Qian T 2025 *Nat. Phys.* **21** 754
[26] Zheng X H, Zheng Z F, Yang S L, Liu C S, Zhang L, and Hao H 2024 *Phys. Rev. B* **110** 115439
[27] Yang S L, Zheng Z F, Hao H, Liu C S, Zheng X H, and Zhang L 2024 *Phys. Rev. B* **110** 235408
[28] Yang Z, Fu X Y, Qin S A, Liu B X, Wang C K, Li Z L, and Qiu S 2025 *Phys. Rev. Appl.* **23** 024041
[29] Li D Z, Li S, Zhong C Y, and He J J 2021 *Nanoscale* **13** 19812
[30] Wang Q H, Bedoya-Pinto A, Blei M, Dismukes A H, Hamo A, Jenkins S, Koperski M, Liu Y, Sun Q C, Telford E J, Kim H H, Augustin M, Vool U, Yin J X, Li L H, Falin A, Dean C R, Casanova F, Evans R F L, Chshiev M, Mishchenko A, Petrovic C, He R, Zhao L, Tsen A W, Gerardot B D, Brotons-Gisbert M, Guguchia Z, Roy X, Tongay S, Wang Z, Hasan M Z, Wrachtrup J, Yacoby A, Fert A, Parkin S, Novoselov K S, Dai P, Balicas L, and Santos E J G 2022 *ACS Nano* **16** 6960
[31] Dong X S, Chen T, Liu G G, Xie L Z, Zhou G H, and Long M Q 2022 *ACS Sens.* **7** 3450
[32] Yao M L, Pan J, Xie W F, Yang Z C, Li M, and Wang H 2023 *Appl. Phys. Lett.* **123** 242405
[33] Yu Y, Liu G G, Luo C, Yang W H, Xiao X B, and Chen T 2023 *ACS Appl. Nano Mater.* **7** 18299
[34] Qi Y P, Sadi M A, Hu D, Zheng M, Wu Z P, Jiang Y C, and Chen Y P 2023 *Adv. Mater.* **35** 2205714
[35] Hu J M, Chen L Q, and Nan C W 2016 *Adv. Mater.* **28** 15
[36] Weng Y K, Lin L F, Dagotto E, and Dong S 2016 *Phys. Rev. Lett.* **117** 037601
[37] Chen J and Dong S 2021 *Phys. Rev. Lett.* **126** 117603
[38] Yang X Y, Ding N, Chen J, Wang Z W, An M, and Dong S 2023 *Appl. Phys. Lett.* **122** 162403
[39] Zhao Y H, Zhang J J, Yuan S J, and Chen Z F 2019 *Adv. Funct. Mater.* **29** 1901420
[40] Ilyas A, Xiang S L, Chen M G, Khan M Y, Bai H, He P M, Lu Y H, and Deng R R 2021 *Nanoscale* **13** 1069
[41] Li Z and Zhou B Z 2020 *J. Mater. Chem. C* **8** 4534
[42] Chen Y, Wang G Z, Guo J T, Li M X, Yuan H K, and Chen H 2024 *ACS Appl. Nano Mater.* **7** 4302
[43] Lee Y B, Hwang Y B, Cho S B, and Chung Y C 2014 *Phys. Chem. Chem. Phys.* **16** 26273
[44] Liu F C, You L, Seyler K L, Li X B, Yu P, Lin J H, Wang X W, Zhou J D, Wang H, He H Y *et al.* 2016 *Nat. Commun.* **7** 12357
[45] Ding W J, Zhu J B, Wang Z, Gao Y F, Xiao D, Gu Y, Zhang Z Y, and Zhu W G 2017 *Nat. Commun.* **8** 14956
[46] Chandrasekaran A, Mishra A, and Singh A K 2017 *Nano Lett.* **17** 3290
[47] Cui C J, Hu W J, Yan X X, Addiego C, Gao W P, Wang Y, Wang Z, Li L Z, Cheng Y C, Li P *et al.* 2018 *Nano Lett.* **18** 1253
[48] Tang X, Shang J, Gu Y T, Du A J, and Kou L Z 2020 *J. Mater. Chem. A* **8** 7331
[49] Chen X F, Ding X K, Gou G Y, and Zeng X C 2024 *Nano Lett.* **24** 3089
[50] Sun X Y, Xia Q, Cao T F, and Yuan S G 2025 *Mater. Sci. Eng., R* **163** 100927
[51] Ju L, Shang J, Tang X, and Kou L Z 2020 *J. Am. Chem. Soc.* **142** 1492
[52] Zheng J D, Zhao Y F, Bao Z Q, Shen Y H, Guan Z, Zhong N, Yue F Y, Xiang P H, and Duan C G 2022 *2D Mater.* **9** 035005
[53] Kresse G and Furthmüller J 1996 *Phys. Rev. B* **54** 11169
[54] Kresse G, Furthmüller J, and Hafner J 1994 *Phys. Rev. B* **50** 13181
[55] Blöchl P E 1994 *Phys. Rev. B* **50** 17953
[56] Kresse G and Joubert D 1999 *Phys. Rev. B* **59** 1758
[57] Perdew J P, Burke K, and Ernzerhof M 1996 *Phys. Rev. Lett.* **77** 3865
[58] Heyd J, Scuseria G E, and Ernzerhof M 2003 *J. Chem. Phys.* **118** 8207
[59] Grimme S, Antony J, Ehrlich S, and Krieg H 2010 *J. Chem. Phys.* **132** 154104
[60] Monkhorst H J and Pack J D 1976 *Phys. Rev. B* **13** 5188
[61] Smidstrup S, Markussen T, Vancraeyveld P, Wellendorff J, Schneider J, Gunst T, Verstichel B, Stradi D, Khomyakov P A, Vej-Hansen U G, Lee M E, Chill S T, Rasmussen F, Penazzi G, Corsetti F, Ojanperä A, Jensen K, Palsgaard M L N, Martinez U, Blom A, Brandbyge M, and Stokbro K 2019 *J. Phys.: Condens. Matter* **32** 015901
[62] Taylor J, Guo H, and Wang J 2001 *Phys. Rev. B* **63** 245407
[63] Tao L L and Wang J 2016 *Appl. Phys. Lett.* **108** 062903
[64] Tsymbal E Y, Mryasov O N, and LeClair P R 2003 *J. Phys.: Condens. Matter* **15** R109